

An Ultra-narrowband, Acoustically Mediated Spintronic Terahertz Emitter

Shihao Zhuang¹, Peter B. Meisenheimer², John T. Heron², Jia-Mian Hu^{1*}

¹*Department of Materials Science and Engineering, University of Wisconsin-Madison, Madison, WI, 53705, USA*

²*Department of Materials Science and Engineering, University of Michigan, Ann Arbor, Michigan, 48109, USA*

Abstract

Narrowband terahertz (THz) radiation are crucial for high-resolution spectral identification, but an intense, narrowband (bandwidth <0.1 THz) THz source driven by a low-cost femtosecond (fs) laser is still missing. Existing fs-laser-driven THz emitters, operating through photoconductive excitation, optical rectification, or ultrafast spin transport (namely, spintronic emitter), are all broadband (bandwidth: 0.3-30 THz). Here, we computationally demonstrate a new type of spintronic emitter that can convert a fs laser pulse into a narrowband THz pulse with an ultra-narrow bandwidth of ~ 0.01 THz. This emitter operates based on the excitation of narrowband THz spin waves in a magnetoelastic film via laser-induced picosecond acoustic pulse, spin current pumping, and spin-to-charge current conversion. Our results also suggest that ultrafast acoustic pulses can enable long-distance (up to millimeters) propagation of THz exchange spin waves that otherwise can only propagate a few nanometers, thus offers new opportunities in the field of THz magnonics as well.

*E-mail: jhu238@wisc.edu

Introduction

The ability to generate terahertz (THz) pulses (electromagnetic waves with a frequency range roughly from 0.1 to 10 THz¹) from femtosecond (fs) laser pulses in visible or near-infrared range^{2,3} is a milestone in THz technology⁴. It has enabled, for example, the development of the THz time-domain spectroscopy (THz-TDS) for spectral identification and imaging of a wide variety of chemical species^{1,5,6}. Notably, THz waves can penetrate many optically opaque packaging materials (e.g., paper, fabric, plastics, among others),^{7,8} making it particularly suited for non-destructive evaluation and security applications.

Photoconductive semiconductors (e.g., GaAs, InAs)⁹⁻¹¹ and electro-optical crystals (e.g., ZnTe, GaP, LiNbO₃)^{9,12,13} are two major types of fs-laser-excited THz emitters. In the former, photoexcited electrons accelerate in a bias electric field, forming a time-varying current which generates THz radiation. In the latter, THz radiation arises from optical rectification. Recently, a third type of fs-laser-excited THz emitter, namely, spintronic THz emitter (STE)^{9,14-22}, has emerged as a promising alternative, due to its low-cost, high intensity, and magnetic-field tunability. A typical STE comprises a ferromagnetic (FM)/heavy-metal(HM) bilayer film grown on a substrate transparent to the incident fs laser (see Fig. 1a). The fs laser pulse irradiates the FM film and generates an ultrafast spin current pulse (duration <1 picosecond) via ultrafast transport of spin-polarized laser-excited electrons^{23,24}. The picosecond (ps) spin current pulse flows from the laser-irradiated surface of the FM film to the HM film. Through the inverse spin Hall effect (iSHE) in the HM, the ps spin current is converted into a ps charge current²⁵, which in turn produces a THz pulse that is often characterized by sampling its electric field component E_{THz} . STEs based on juxtaposed ferrimagnetic (or antiferromagnetic) metals and HM have also been demonstrated²⁶⁻²⁸. The THz pulse generated from such STE typically has a relatively broad bandwidth (>0.2 THz) associated with the single-cycled transient spin current pulse, which hinders high-spectral-resolution identification and imaging.

In this article, we design and computationally demonstrate an acoustically mediated spintronic emitter (acousto-STE) that can emit THz pulse with an ultra-narrow bandwidth (~ 0.01 THz). Figure 1b shows the structure of the proposed emitter. The fs laser passes through the transparent substrate and irradiates the bottom surface of a metallic transducer. This will inject a ps longitudinal acoustic strain pulse $\varepsilon_{zz}(t)$ into the adjacent thermal insulation layer²⁹. Importantly,

we show that this optically induced ps acoustic pulse can excite multi-mode, narrowband THz spin waves in the overlaying magnetoelastic film. Through spin pumping³⁰, the THz spin waves on the magnetic film surface further injects a ps spin current into the HM capping layer, where it is then converted to a ps charge current via the iSHE and thus the THz emission.

Device Design

A MgO(substrate)/Fe(20 nm)/MgO(400 nm)/Fe_{79.5}Ga_{20.5}(100 nm)/Pt(5 nm) multilayer is considered as a model system for the proposed acoustically mediated spintronic emitter, as shown in Fig. 2a. The Fe_{79.5}Ga_{20.5} (FeGa) film displays a strong magnetoelastic coupling,^{31,32} and is desirably thick enough to allow for sufficient coupling between the injected elastic wave and the local magnetization. Pt is selected as the HM capping layer due to its large spin Hall angle, excellent electrical conductivity, and chemical stability. The Pt should at least be thicker than its spin diffusion length l_{sd} (~ 3.4 nm³³), otherwise a large portion of the spin current in Pt will be reflected from its top surface and cancels out the inflow of spin current. The (001) MgO film plays four major roles. First, it acts as a thermal insulation layer to shield the FeGa film from most or all of the heat deposited into the metallic Fe transducer, thereby excluding the influence of heating on the spin wave generation; Second, the (001) MgO film also provides a template for the epitaxial growth of (001) FeGa (see Supplementary Information 1). Third, although the fs laser will also trigger the ultrafast transport of spin-polarized electrons in the Fe transducer (like in conventional spintronic emitters), the dielectric MgO will block the transport of these electrons into the FeGa. Otherwise, the magnetization in FeGa may be subject to spin-transfer torques. Finally, the MgO layer is also utilized to delay the arrival of the elastic wave at the bottom surface of FeGa film (a 400-nm-thick MgO film will cause a delay of 44 ps). Since the laser-induced ultrafast demagnetization in Fe alone can generate pulsed THz radiation within the first 5~10 ps after pumping³⁴, adding a controllably delay can ensure the sampled free-space E_{THz} signals are predominantly caused by elastic wave injection.

Spin Wave Excitation and The Mechanisms

Consider the incident laser (wavelength: 800 nm; duration: 60 fs; absorbed fluence: 5 mJ/cm²) irradiates the entire bottom surface of the Fe (Fig. 2a). A (001) Fe film exhibits an absorption length of ~ 17.5 nm to the 800-nm-wavelength laser. Thus, a 20-nm-thick (001) Fe film should absorb the majority of incident photons. The laser-excited hot electrons then quickly exchange

energy with the phonons, leading to a rapid rise in the lattice temperature of Fe. As a result, longitudinal elastic wave $\varepsilon_{zz}(t)$ will be injected from the Fe into both the MgO film and the MgO substrate through the thermal expansion of Fe. In parallel, heat transport from the hotter Fe to the MgO begins. We describe these coupled processes by coupling the classical two-temperature model^{29,35} with the heat transport equation (see Methods). Figure 2b shows the calculated profiles of lattice temperature T_1 and longitudinal strain ε_{zz} across the MgO(substrate)/Fe/MgO(film) tri-layer at 10, 20, and 30 ps after irradiation. The elastic wave will then travel into the FeGa and then Pt. When elastic wave reaches the stress-free top surface of Pt, it will be reflected back into the FeGa. A smaller-magnitude backward elastic wave will arise every time the elastic wave travels across an interface. Figure 2c and 2d shows the propagation of the incoming elastic wave $\varepsilon_{zz}(z, t)$ and the excited spin wave $\Delta m_z(z, t)$ inside the FeGa layer, respectively. Comparing Figs. 2c and 2d, it can be seen that the spin wave was generated from the bottom FeGa surface almost at the same moment when the elastic wave $\varepsilon_{zz}(t)$ travels into the FeGa ($t=0$ ps). However, the spin wave arrives at the top FeGa surface at $t\sim 10$ ps while the acoustic wave arrives at $t\sim 20$ ps.

Figure 3a shows the frequency spectra of the spin wave $\Delta m_z(z, t)$, where the frequency represents the precession frequency of local magnetization. As seen, although the precession frequencies are primarily distributed at frequencies below 0.2 THz, strong peaks emerge near 0.7 THz as well. The strong preference of the spin waves in selecting a few particular frequencies lead to a narrow bandwidth for each spin wave mode. As shown in Fig. 3b, the frequency-wavenumber relation $\omega(k)$ of the spin wave displays both a linear and parabolic curve. Among them, the linear $\omega(k)$ well fits the analytical formula $\omega = v_s k$ (dashed straight line), where v_s is the longitudinal sound velocity in FeGa (i.e., the velocity of elastic wave). This means that all the spin wave components travel at the same phase velocity as the sound velocity, implying a pure magnetoelastic excitation mechanism. For clarification, we perform a control simulation by setting the exchange coupling coefficient A_{ex} to be zero. As shown in Fig. 3c, the simulated $\omega(k)$ displays an expected linear relation $\omega = v_s k$, and the precession frequency remains below 0.2 THz due to the relatively low frequency of the elastic waves.

The parabolic relation $\omega(k)$ shown in Fig. 3b well fits the analytical formula $\omega = \frac{\gamma}{1+\alpha^2} \frac{2A_{\text{ex}}}{\mu_0 M_s} k^2$ (dashed curve), which is derived by linearizing the magnetization dynamics equation

in the presence of only the magnetic exchange coupling field \mathbf{H}^{exch} (Supplementary Information 2). Here γ is gyromagnetic ratio; α is damping coefficient; μ_0 is vacuum permeability; M_s is saturation magnetization. Therefore, spin waves displaying such parabolic relation $\omega(k)$ are excited by exchange coupling. Among them, the low-frequency (<0.2 THz) exchange spin waves are secondary waves that do not interact with the elastic wave. To demonstrate this, we perform 2D fast Fourier transform (FFT) for the simulated $\Delta m_z(z,t)$ over the time period from $t=70$ ps to $t=125$ ps, during which there are no strong elastic waves in the FeGa (see Fig. 2c). The resultant $\omega(k)$, as plotted in Fig. 3d, well matches the analytically derived parabolic relation, and the precession frequencies are all below 0.2 THz.

The high-frequency (near 0.7 THz) exchange spin waves, by contrast, arise due to the strong interaction with the elastic waves. Specifically, once the magnetization vector at the bottom surface of the FeGa ($z=0$) is reoriented by the incoming elastic wave via magnetoelastic coupling, the nearest magnetization vector will be subsequently reoriented by the \mathbf{H}^{exch} , and so forth for the second nearest magnetization vector, leading to the excitation of an exchange spin wave. As elastic wave propagates across the FeGa, it will constantly trigger the excitation of exchange spin waves from the frontmost position of its waveform. This can be seen from Fig. 3e, which simultaneously shows the real-space profiles of the spin wave (red shades) and the elastic wave (blue shades) within the first 10 ps with a 2-ps-interval across the FeGa. The phase velocity of these elastically initiated exchange spin waves, given by $v_p = \omega^*/k^* = \frac{\gamma}{1+\alpha^2} \frac{2A_{\text{ex}}}{\mu_0 M_s} k^*$, is equal to the velocity of the elastic wave v_s . This allows us to calculate the wavenumber k^* and center frequency f^* analytically,

$$k^* = \frac{v_s}{2\pi} \frac{1 + \alpha^2 \mu_0 M_s}{\gamma 2A_{\text{ex}}}; f^* = \frac{v_s^2}{2\pi} \frac{1 + \alpha^2 \mu_0 M_s}{\gamma 2A_{\text{ex}}}. \quad (1)$$

In FeGa, $v_s = \sqrt{c_{11}/\rho}=4974$ m/s, where c_{11} and ρ are the elastic stiffness coefficient and mass density, respectively. Plugging in the numbers of other parameters (Methods), one has $k^* \sim 147.42 \mu\text{m}^{-1}$ and $f^* \sim 0.73$ THz, which are consistent with the presence of strong peaks at ~ 0.7 THz in the simulated $\omega(k)$. The group velocity v_g of these elastically initiated exchange spin wave, given by $v_g = \partial\omega/\partial k|_{k=k^*}$, is calculated to be 9948 m/s. This is exactly twice the sound velocity v_s , which

explains why it takes ~ 10 ps (≈ 100 nm /9948 m/s) for the spin wave to arrive at the FeGa top surface (Fig. 2d), while the arrival of the elastic wave takes ~ 20 ps (Fig. 2c).

Tuning the Frequency

The ability to tune the center frequency of a narrowband THz pulse will expand its application by enabling the identification of many more species. Equation (1) indicates that the center frequency (f^*) of the elastically initiated exchange spin waves can be tuned by modifying the properties of the magnetoelastic film. Figure 4a shows the variation of the f^* with both the A_{ex} and M_s from numerical simulations. The variation of f^* becomes smaller at larger A_{ex} , yet in all cases, the simulated f^* agree well with those calculated via Eq. (1), as shown in Fig. 4b. This further corroborates the validity of Eq. (1). The top panel of Fig. 4c show the frequency spectra of such elastically initiated exchange spin waves simulated under two different M_s at $A_{\text{ex}}=10$ pJ/m, where the peaks at the f^* are denoted by red dots. The bottom panel of Fig. 4c show their real-space profiles, displaying a wavelength ($=1/k^*$) of ~ 7 nm (3.5 nm) for $M_s=0.65$ MA/m (1.30 MA/m). Figure 4d lists the f^* for commonly used magnetoelastic materials, calculated via Eq. (1) based on experimentally measured parameters (listed in Supplementary Information 3).

Spin Current Injection and Spin-to-Charge Current Conversion

The precession of magnetization at the FeGa top surface ($\mathbf{m}(z = 100 \text{ nm}, t)$, denoted as $\mathbf{m}^0(t)$) allows for transferring angular momentum to the adjacent Pt, known as spin pumping³⁰. Due to the iSHE of the Pt, the injected spin current, which is perpendicular to the FeGa/Pt interface (along z), is converted to a charge current flowing parallel to the FeGa/Pt interface. Due to spin diffusion, the magnitude of spin current in the Pt decreases monotonically away from its source and eventually to zero if the Pt thickness is significantly larger than its spin diffusion length. The charge current in Pt scales linearly with the spin current. The charge current J_c is predominantly contributed by terms associated with the magnetoelastic field $\mathbf{H}_{\text{mel}}^0$ and the exchange coupling field $\mathbf{H}_{\text{exch}}^0$ at the FeGa top surface, that is, $J_c \approx J_{c,\text{mel}} + J_{c,\text{exch}}$, which is demonstrated in Fig. 5a.

Specifically, the temporal variation of x -component of $J_{c,\text{mel}}$ is mainly determined by the temporal variation of longitudinal strain $\varepsilon_{zz}^0(t)$ (see Methods),

$$J_{c,\text{mel}}^x(z, t) \approx -\frac{2B_1}{\mu_0 M_s} k_0(z) m_{y,\text{init}}^0 (m_{z,\text{init}}^0)^2 \varepsilon_{zz}^0(t), \quad (2)$$

where B_1 is the magnetoelastic coupling coefficient; $m_{y,\text{init}}^0$ and $m_{z,\text{init}}^0$ are the initial ($t=0$) magnetization at the FeGa top surface. Equation (2) indicates that the frequency spectra of $\langle J_{c,\text{mel}}^x \rangle(t)$ should be nearly the same as that of $\varepsilon_{zz}^0(t)$. This can be seen from the middle panel of Fig. 5b. By decomposing the time-varying \mathbf{m}^0 into a series of sinusoidal waves of different amplitudes $\Delta\mathbf{m}_q^0$, frequencies ω_q and wavenumbers k_q , i.e., $\mathbf{m}^0(t) = \mathbf{m}_{\text{init}}^0 + \sum_q \Delta\mathbf{m}_q^0 e^{i(k_q z - \omega_q t)}$, the temporal variation of x -component of $J_{c,\text{exch}}$ can be approximated as,

$$J_{c,\text{exch}}^x(z, t) \approx -\frac{2A_{ex}}{\mu_0 M_s} k_0(z) \sum_q (\Delta\mathbf{m}_q^0 \cdot \mathbf{R}) k_q^2 e^{i(k_q z - \omega_q t)}, \quad (3)$$

where \mathbf{R} is a vector with non-zero fixed coefficients (see Eqs. 16 and 17 in Methods). Equation (3) indicates that the peaks in the frequency spectra of $\mathbf{m}^0(t)$ and $\langle J_{c,\text{exch}}^x \rangle(t)$ should appear at the same frequencies ω_q . Further, it establishes a quantitative relationship between the peak amplitude of the surface spin wave $\Delta\mathbf{m}_q^0$ and that of the $J_{c,\text{exch}}^x$, i.e., $(\Delta\mathbf{m}_q^0 \cdot \mathbf{R}) k_q^2$, respectively. Applying the parabolic dispersion relation $\omega_q \propto k_q^2$ of exchange spin waves, one has $(\Delta\mathbf{m}_q^0 \cdot \mathbf{R}) k_q^2 \propto (\Delta\mathbf{m}_q^0 \cdot \mathbf{R}) \omega_q$. Consequently, higher-frequency peaks tend to have higher peak amplitudes in the frequency spectrum of $\langle J_{c,\text{exch}}^x \rangle(t)$. This can be seen from the bottom panel of Fig. 5b.

Furthermore, comparing the frequency spectra of J_c^x , J_{mel}^x , and J_{exch}^x in Fig. 5b, it can be seen that the high-frequency (~ 0.7 THz) components of J_c^x are completely contributed by the high-frequency components of J_{exch}^x . A larger, faster-rising acoustic strain pulse, which can be obtained using relatively thin Fe transducer (see Supplementary Information 4), can rotate the magnetization at the frontmost position of the elastic wave by a greater extent, leading to a larger spatial variation of the local magnetization near the FeGa film surface and thus a larger $\mathbf{H}_{\text{exch}}^0$. This in turn yields a larger J_{exch}^x and hence the J_c^x , as shown in Supplementary Information 5.

Emission of pulsed THz electric field

Time-varying charge currents $\mathbf{J}_c(t)$ in the Pt leads to the emission of electromagnetic waves. Figure 6a-b show the emitted electric-field component $E_{\text{THz}}^x(t)$ and its frequency spectrum, respectively, from our acoustically mediated spintronic emitter (acousto-STE). The average emitted THz power, calculated based on the $E_{\text{THz}}(t)$ within the first 40 ps, is $\sim 178 \mu\text{W}$, which is at the same scale as the commercial photoconductive emitters ($40 \mu\text{W}$, ref. ³⁶) and the optical-

rectification based ones (150 μW , ref. ³⁷). The bandwidths at the three highest peaks (indicated by red dots, Fig. 6b) in the THz spectra are all ~ 0.01 THz. As shown in Fig. 6c, this bandwidth is at least one order of magnitude smaller than fs-laser-excited THz emitters based on photoconductive switch⁹⁻¹¹ or optical rectification^{9,12,13}, as well as the conventional spintronic THz emitter^{9,14,15,21,26}.

It is worth noting that, in a conventional spintronic emitter, the spin current originates from the laser-irradiated surface of the metallic magnet, and is a single-cycled transient typically with < 1 ps in duration¹⁴. In our acoustically mediated spintronic emitter, the spin current originates from the magnet/heavy-metal interface, where the magnet can be either metallic or insulating. The spin/charge current displays a rather complex waveform over a more extended period of time (\sim tens of ps, Fig. 5a). The spectral features of the spin current are dictated by the spectral features of the spin waves in the magnet. Therefore, it is the narrowband THz spin wave excitation that eventually leads to the narrowband THz radiation. The narrow bandwidth of THz spin wave spectra mainly results from the highly discrete and selective frequency modes (see discussion on the mechanism of spin wave excitation in Fig. 3). In addition, there exist strong interference among the spin wave components due to (1) spin wave is confined within the two surfaces of FeGa film and (2) the traveling elastic wave is constantly initiating new exchange spin waves. This leads to significant frequency splitting which reduces the bandwidth even further.

Concluding Remarks

In summary, we computationally demonstrate a fs-laser-excited emitter that can provide multi-mode, narrowband THz pulse with bandwidths ~ 0.01 THz, based on the acoustic excitation of multi-mode, narrowband THz spin waves. The average power of the emitted THz pulse (~ 178 μW) is at the same scale as commercial fs-laser-excited broadband THz emitters. The principles of tuning the center frequency of the exchange-coupling-based THz spin waves by modulating relevant materials parameters are established by deriving a simple analytical formula (Eq. 1), whose validity is corroborated by numerical simulations. Based on this formula, we show that the center frequency can be broadly tuned within the range of 0.6–2.6 THz by selecting an appropriate magnetoelastic material (Fig. 4d).

Overall, we discover a route to generate an intense, narrowband THz pulse through fs laser excitation, which has previously not been possible. Such narrowband THz pulses are crucial for high-spectral-resolution identification and imaging¹. Beyond the THz technology, our

computations reveal an approach to optically excite THz exchange spin waves of wide-ranging center frequencies in commonly used magnetoelastic materials. In particular, this approach also enables an extremely-long-distance (up to millimeters) propagation of these THz exchange spin waves, by constantly initiating new THz exchange spin waves from the frontmost position of a travelling elastic wave (Fig. 3e). This in effect extends the propagation length of such THz exchange spin waves to that of elastic waves, which can be up to millimeters or longer. For example, if using a 1-micron-thick FeGa, such THz exchange spin wave can in effect propagate 1 micron and then keep propagating along the opposite direction, and so forth, until the elastic wave vanishes. This new concept of achieving non-local transport of THz exchange spin waves, which by themselves can only propagate a few nanometers before the decay into other lower-energy spin waves³⁸, can be used to design new prototypes of THz magnonic³⁹ and spin-caloritronic⁴⁰ devices.

Acknowledgements

The work is supported by a start-up fund from the University of Wisconsin–Madison. The simulations were performed using Bridges at the Pittsburgh Supercomputing Center through allocation TG-DMR180076, which is part of the Extreme Science and Engineering Discovery Environment (XSEDE) and supported by NSF grant ACI-1548562. The work at University of Michigan is supported by NSF CAREER grant DMR-1847847.

Methods

Our in-house Multiphysics model simultaneously considers the following three coupled kinetic processes that have previously not been considered together: (1) the generation of ultrafast acoustic pulses by fs laser excitation; (2) acoustic excitation of spin waves in magnetic multilayer heterostructures; (3) heat transport in magnetic multilayers. Once the evolution of local magnetization vector at the ferromagnet/heavy-metal interface (FeGa/Pt herein) is calculated, we can then calculate the spin current pumped from the interface into the Pt, followed by the conversion of the spin current to the charge current, and finally the electric-field component of the electromagnetic wave emitted by the time-varying charge current.

Upon the excitation by the fs laser, the evolution of the electron temperature T_e and lattice temperature T_l in the (001) Fe are described by the classical two-temperature model (2TM),^{29,35}

$$c_e \frac{\partial T_e}{\partial t} = \frac{\partial}{\partial z} \left(\kappa_e \frac{\partial T_e}{\partial z} \right) - G(T_e - T_l) + S(z, t), \quad (4)$$

$$c_l \frac{\partial T_l}{\partial t} = G(T_e - T_l) + \frac{\partial}{\partial z} \left(\kappa_l \frac{\partial T_l}{\partial z} \right). \quad (5)$$

Here $c_e = \eta_e T_e$ is the electronic specific heat, which is a function of T_e with a pre-factor η_e ; c_l is the lattice specific heat and is a function of T_l ; $\kappa_e = \frac{T_e}{T_l} \kappa_l$ is the thermal conductivity of the electron gas, where κ_l is the lattice thermal conductivity and is a function of T_l ; G is the electron-phonon coupling coefficient, describing the efficiency of energy transfer between the electronic and lattice subsystems. These materials parameters are all for (001) Fe. $S(z, t) = \frac{Q}{\xi} \exp(-z/\xi) I(t)$ is the source term describing the local rate of energy production in the electron subsystem due to laser irradiation, where Q is absorbed laser fluence ($=5 \text{ mJ/cm}^2$); ξ is the absorption length of the metallic transducer Fe to the incident laser ($\xi = 17.5 \text{ nm}$ for an 800-nm-wavelength laser); $I(t) = \frac{1}{2\tau_L \cosh(1.76t/\tau_L)^2}$ describes the temporal profile of the laser pulse, and τ_L is pulse duration ($=60 \text{ fs}$).

It is worth noting that the 2TM has been successfully used to fit the experimentally measured data of fs-laser-excited ps acoustic pulses in a (001)Fe/MgO(substrate) bilayer heterostructure.⁴¹ For the proposed MgO(substrate)/Fe/MgO(film)/FeGa/Pt multilayer stack, the laser excitation leads to a rapid increase in the T_e of (001) Fe, described by Eq. (4). The hot electrons then transfer their energy to the Fe lattice through electron-phonon coupling, thereby increasing the lattice temperature T_l of Fe, described by Eq. (5). The heat transport from the heated Fe transducer to both the underlying MgO substrate and overlaid MgO film (see profile of T_l in the top panel of Fig. 2a) is modelled by coupling Eq. 5 (solved only in Fe) with the classical heat transport equation (solved in all remaining layers),

$$c_l \frac{\partial T_l}{\partial t} = \frac{\partial}{\partial z} \left(\kappa_l \frac{\partial T_l}{\partial z} \right). \quad (6)$$

Here we assume that T_l is spatially uniform in the xy plane and solve for the $T_l(z, t)$ only. c_l and κ_l are the lattice specific heat and lattice thermal conductivity, both of which are set to be different

in different layers (MgO, FeGa, Pt) and vary with the local T_l . The heat flow continuity boundary condition is applied at all interfaces. The top surface of Pt and the bottom surface of MgO substrate are both set to be thermally insulating.

The rise in both the electron and lattice temperature will induce stress. However, since MgO is electronically insulating, laser-excited hot electrons in Fe cannot diffuse into the MgO, leaving the electron temperature of the MgO unchanged. In other words, although both the lattice and electronic thermal stress are induced in the Fe, only lattice thermal stress exists in the MgO layer. The thermal stress in the FeGa and Pt layer are zero, because both the electron and lattice temperature in these two materials remain unaffected during the entire process of converting the fs laser pulse into a THz pulse, which completes within ~ 125 ps after the laser excitation. The thermal stress generated in the MgO/Fe/MgO trilayer will launch a longitudinal elastic wave $\varepsilon_{zz}(z, t)$ from the Fe/MgO interfaces, which propagate into both the MgO substrate and film the multilayer stack. In particular, once the elastic wave travels into the magnetoelastic FeGa and excites spin wave (Fig. 2d), the backaction of local magnetization dynamics will generate a small secondary elastic wave due to the magnetostrictive stress.⁴² These processes can be modelled by solving a generalized elastodynamic equation that incorporates the lattice and electronic thermal stress as well as the magnetostrictive stress, given by,

$$\rho \frac{\partial^2 \mathbf{u}_x}{\partial t^2} = \mathbf{c}_{44} \frac{\partial^2 \mathbf{u}_x}{\partial z^2} + B_2 \frac{\partial(\mathbf{m}_x \mathbf{m}_z)}{\partial z}, \quad (7)$$

$$\rho \frac{\partial^2 \mathbf{u}_y}{\partial t^2} = \mathbf{c}_{44} \frac{\partial^2 \mathbf{u}_y}{\partial z^2} + B_2 \frac{\partial(\mathbf{m}_y \mathbf{m}_z)}{\partial z}, \quad (8)$$

$$\rho \frac{\partial^2 \mathbf{u}_z}{\partial t^2} = \mathbf{c}_{11} \frac{\partial^2 \mathbf{u}_z}{\partial z^2} + B_1 \frac{\partial(\mathbf{m}_z^2)}{\partial z} - (\mathbf{c}_{11} + 2\mathbf{c}_{12})\beta \frac{\partial T_l}{\partial z} - \frac{2}{3} c_e \frac{\partial T_e}{\partial z}, \quad (9)$$

where ρ is the mass density; \mathbf{c}_{11} , \mathbf{c}_{12} and \mathbf{c}_{44} are the elastic stiffness coefficients; β is the linear thermal expansion coefficient. ρ , \mathbf{c} , and β are all set to be different in different layers; \mathbf{c} and β are further set to be a function of T_l . The last term in the Eq. (9), $\frac{2}{3} c_e \frac{\partial T_e}{\partial z}$, describes the stress contributed by free electron gas²⁹. $B_1 = -1.5\lambda_{100}(c_{11}^{\text{FeGa}} - c_{12}^{\text{FeGa}})$ and $B_2 = -3\lambda_{111}c_{44}^{\text{FeGa}}$ are the magnetoelastic coupling coefficients of the FeGa film (λ_{100} and λ_{111} are its magnetostrictive coefficients); $\mathbf{m}=\mathbf{M}/M_s$ is the normalized local magnetization vector (M_s is the saturation magnetization of FeGa). The stress continuity boundary condition is applied at all interfaces. The

bottom surface of MgO substrate and top surface of Pt are set to be stress-free. From Eq. (9), it can be seen that longitudinal elastic wave $\varepsilon_{zz}(z, t)$ in the FeGa should include a magnetoelastic feedback from time-varying magnetization.^{39,42} We extracted such secondary elastic wave by calculating the difference in two groups of $\varepsilon_{zz}(z, t)$ simulated under a non-zero and zero magnetostriction. It is found that such secondary elastic wave has a significantly smaller magnitude ($\sim 10^{-6}$) than the injected elastic wave ($\sim 10^{-3}$), its influence can therefore be omitted.

The evolution of local magnetization $\mathbf{m}(z, t)$ in FeGa is modelled by solving the Landau-Lifshitz-Gilbert (LLG) equation,

$$\frac{\partial \mathbf{m}}{\partial t} = -\frac{\gamma}{1 + \alpha^2} \mathbf{m} \times \mathbf{H}_{\text{eff}} - \frac{\alpha\gamma}{1 + \alpha^2} \mathbf{m} \times (\mathbf{m} \times \mathbf{H}_{\text{eff}}). \quad (10)$$

The total effective magnetic field \mathbf{H}_{eff} is contributed by the magnetocrystalline anisotropy field \mathbf{H}^{anis} , magnetic exchange coupling field \mathbf{H}^{exch} , magnetoelastic anisotropy field \mathbf{H}^{mel} , magnetic dipolar coupling field \mathbf{H}^{dip} , and the external magnetic field \mathbf{H}^{ext} . For epitaxial (001) FeGa with a cubic paramagnetic phase, one has ($i = x, y, z$, and $j \neq i, k \neq i, j$),

$$H_i^{\text{anis}} = -\frac{2}{\mu_0 M_s} [K_1(m_j^2 + m_k^2) + K_2 m_j^2 m_k^2] m_i, \quad (11)$$

$$H_i^{\text{mel}} = -\frac{1}{\mu_0 M_s} [2B_1 m_i \varepsilon_{ii} + B_2 (m_j \varepsilon_{ij} + m_k \varepsilon_{ik})], \quad (12)$$

where μ_0 is vacuum permeability; K_1 and K_2 are magnetocrystalline anisotropy coefficients; strain $\varepsilon_{ij} = \frac{1}{2} (\frac{\partial u_i}{\partial j} + \frac{\partial u_j}{\partial i})$. Since the optically excited acoustic wave in the MgO(substrate)/Fe/MgO multilayer only contains the longitudinal component ε_{zz} , at the moment the acoustic wave travels into the FeGa, the magnetoelastic field in the FeGa is given by $(H_x^{\text{mel}}, H_y^{\text{mel}}, H_z^{\text{mel}}) = (0, 0, -\frac{2B_1}{\mu_0 M_s} m_z \varepsilon_{zz})$. Therefore, the initial magnetization state of the FeGa must have a nonzero out-of-plane component ($m_z \neq 0$), otherwise the $\varepsilon_{zz}(t)$ cannot interact with the local magnetization in the FeGa. One must also ensure that the initial magnetization has a nonzero in-plane component ($m_x \neq 0$ or $m_y \neq 0$), in other words, the initial magnetization cannot be perfectly aligning along the z -axis, otherwise the torque $\mathbf{m} \times \mathbf{H}^{\text{mel}} (= m_z \times H_z^{\text{mel}})$ would be zero and hence \mathbf{m} would not evolve. Thus, we introduce a bias dc magnetic field applied along the z -direction ($\mathbf{H}^{\text{ext}} = H_z^{\text{ext}}$) to obtain a tilted, spatially uniform initial magnetization \mathbf{m} in an otherwise in-plane

magnetized FeGa film. It was found that the generated spin current is the largest when the initial \mathbf{m} is $\sim 45^\circ$ off the film plane (Supplementary Information 6). The magnetic exchange coupling field $\mathbf{H}^{\text{exch}} = \frac{2A_{\text{ex}}}{\mu_0 M_s} \nabla^2 \mathbf{m}$. For an infinitely large xy plane within which the magnetization \mathbf{m} is spatially uniform, the dipolar coupling field is calculated as $\mathbf{H}^{\text{dip}} = (0, 0, -M_s m_z)$, which is numerically validated (Supplementary Information 7).

The material parameters for Fe are:⁴³⁻⁴⁹ $\rho_{\text{Fe}} = 7870 \text{ kg}\cdot\text{m}^{-3}$, $\eta_e = 702 \text{ J}\cdot\text{K}^{-2}\cdot\text{m}^{-3}$, $G = 5.48 \times 10^{18} \text{ W}\cdot\text{K}^{-1}\cdot\text{m}^{-3}$, the room temperature (298K), $\mathbf{c}_{11}^{\text{Fe}} = 226 \text{ GPa}$, $\mathbf{c}_{12}^{\text{Fe}} = 140 \text{ GPa}$, $\mathbf{c}_{44}^{\text{Fe}} = 116 \text{ GPa}$, $c_l^{\text{Fe}} = 25.1 \text{ J}\cdot\text{mol}^{-1}\text{K}^{-1}$, $\kappa^{\text{Fe}} = 72.4 \text{ W}\cdot\text{m}^{-1}\text{K}^{-1}$, $\beta^{\text{Fe}} = 11.6 \times 10^{-6} \text{ K}^{-1}$. For MgO,^{50,51} $\rho_{\text{MgO}} = 3580 \text{ kg}\cdot\text{m}^{-3}$, at room temperature, its $\mathbf{c}_{11}^{\text{MgO}} = 297 \text{ GPa}$, $\mathbf{c}_{12}^{\text{MgO}} = 95.9 \text{ GPa}$, $\mathbf{c}_{44}^{\text{MgO}} = 156 \text{ GPa}$, $c_l^{\text{MgO}} = 37.4 \text{ J}\cdot\text{mol}^{-1}\text{K}^{-1}$, $\kappa^{\text{MgO}} = 50.1 \text{ W}\cdot\text{m}^{-1}\text{K}^{-1}$, $\beta^{\text{MgO}} = 10.5 \times 10^{-6} \text{ K}^{-1}$. In MgO and Fe, elastic stiffness, heat capacity, heat conductivity, and thermal expansion coefficient are considered temperature dependent, specifically, by fitting data with third- or fourth-degree polynomial function of temperature. For FeGa,^{31,39,52} $\rho_{\text{FeGa}} = 7800 \text{ kg}\cdot\text{m}^{-3}$, at room temperature, $\mathbf{c}_{11}^{\text{FeGa}} = 193 \text{ GPa}$, $\mathbf{c}_{12}^{\text{FeGa}} = 155 \text{ GPa}$, $\mathbf{c}_{44}^{\text{FeGa}} = 122 \text{ GPa}$, $M_s = 1.2 \times 10^6 \text{ A/m}$ (from our own measurement), $\gamma = 2.25 \times 10^5 \text{ m}\cdot\text{s}^{-1}\cdot\text{A}^{-1}$, cubic magnetocrystalline anisotropy constant $K_1 = 636 \text{ J}\cdot\text{m}^{-2}$ (from our own measurement), exchange coupling constant $A_{\text{ex}} = 1.8 \times 10^{-11} \text{ J}\cdot\text{m}^{-1}$, $\alpha = 0.017$, $\lambda_{100} = 1.5 \times 10^{-4}$, $\lambda_{111} = 2.8 \times 10^{-5}$. For Pt,⁵³ $\rho_{\text{Pt}} = 21400 \text{ kg}\cdot\text{m}^{-3}$, $\mathbf{c}_{11}^{\text{Pt}} = 347 \text{ GPa}$, $\mathbf{c}_{12}^{\text{Pt}} = 250 \text{ GPa}$, $\mathbf{c}_{44}^{\text{Pt}} = 75 \text{ GPa}$;

When numerically solving Eqs. (4-10), the MgO(1000 nm)/Fe(20 nm)/MgO(400 nm)/FeGa(100 nm)/Pt(5 nm) stack is discretized into one-dimensional (1D) computational cells along z direction, with cell size $\Delta z = 0.5 \text{ nm}$. The MgO substrate is thick enough to ensure that the optically injected elastic wave is not reflected back at bottom surface of the substrate and arrive the bottom surface of the Fe transducer within $\sim 125 \text{ ps}$ after the laser excitation (i.e., the time required for completing the conversion of fs optical pulse to THz pulse). Central finite difference is used for calculating spatial derivatives. Eqs. (4-10) are coupled with each other and solved simultaneously, classical Runge-Kutta method is used for time-marching with a real-time step $\Delta t = 0.01 \text{ fs}$. The same results are obtained from simulations with $\Delta t = 0.005 \text{ fs}$. Appropriate thermal, magnetic, and mechanical boundary conditions are implemented on all surfaces and interfaces. These include (i) temperature continuity and heat flow continuity, $T^A = T^B$, $\kappa^A \partial T^A / \partial \mathbf{n} = \kappa^B \partial T^B / \partial \mathbf{n}$, where \mathbf{n} is the normal vector of an interface or surface; (ii) the free magnetic boundary condition

$\partial \mathbf{m} / \partial \mathbf{n} = 0$ at the top and bottom surface of the magnetic layer, which leads to the reflection of the excited spin waves between its two surfaces; (iii) displacement continuity and stress continuity, $\mathbf{u}^A = \mathbf{u}^B$, $\boldsymbol{\sigma}^A = \boldsymbol{\sigma}^B$; superscripts ‘A,B’ denote different materials. In particular, by setting the heat flow or stress in the air to be zero, the continuity boundary condition is converted to a thermal insulation boundary condition, e.g., $\partial T^A / \partial \mathbf{n} = 0$, or a stress-free boundary condition $\boldsymbol{\sigma}^A = 0$ (precisely, $\sigma_{iz}^A = 0$ at the outermost layer, $i=x,y,z$) which leads to the reflection of elastic wave from the Pt top surface.

The numerical validity of our in-house simulation codes was demonstrated using specifically designed test problems, where results obtained from our codes agree well with those from the finite-element-method based solvers in commercial software COMSOL Multiphysics (Supplementary Information 8).

Calculation of spin current and charge current in Pt

The spin current density generated at the FeGa/Pt interface $\mathbf{J}_s^0(z=t_{\text{FeGa}}, t)$ can be calculated as $\mathbf{J}_s^0 \approx \frac{\hbar}{4\pi} \text{Re}[g_{\uparrow\downarrow}^r] \left(\mathbf{m}^0 \times \frac{\partial \mathbf{m}^0}{\partial t} \right)$,^{30,33} where t_{FeGa} is the thickness of FeGa (100 nm); $\mathbf{m}^0(t)$ refers to the time-varying local magnetization vector at $z=t_{\text{FeGa}}$; $\text{Re}[g_{\uparrow\downarrow}^r]$ is the real part of the reflection spin mixing conductance, taken as $2.1 \times 10^{19} \text{ m}^{-2}$.³³ The spin current will then decay along the thickness direction of the Pt due to spin relaxation and diffusion, and the dc component of the spin current is given by,^{33,42}

$$\mathbf{J}_s(z, t) = \mathbf{J}_s^0(t) f(z) = \mathbf{J}_s^0(t) \frac{\sinh\left(\frac{t_{\text{FeGa}} + t_{\text{Pt}} - z}{l_{sd}}\right)}{\sinh\left(\frac{t_{\text{Pt}}}{l_{sd}}\right)} \quad (13)$$

where t_{Pt} is thickness of the Pt film and $l_{sd} = 3.4 \text{ nm}$ is the spin diffusion length of Pt.⁵⁴ The spin current in the Pt, $\mathbf{J}_s(z, t)$, will then be converted into a charge current $\mathbf{J}_c(z, t)$ via the inverse spin Hall effect,⁵⁴ given by, $\mathbf{J}_c(z, t) = \alpha_{\text{SH}} \frac{2e}{\hbar} \mathbf{e}_s \times \mathbf{J}_s(z, t)$, where $\alpha_{\text{SH}} = 0.056$ is the spin Hall angle of Pt,²⁵ \mathbf{e}_s is the unit vector in the direction of spin current in the Pt. Since \mathbf{e}_s is perpendicular to the FeGa/Pt interface, the charge current is parallel to the interface, with $J_c^x(z, t) = -\alpha_{\text{SH}} \frac{2e}{\hbar} J_s^y(z, t)$; $J_c^y(z, t) = \alpha_{\text{SH}} \frac{2e}{\hbar} J_s^x(z, t)$.

Note that the generated charge currents in the Pt can be written as the sum of charge currents contributed by each effective magnetic field, $\mathbf{J}_c = \mathbf{J}_{c,\text{anis}} + \mathbf{J}_{c,\text{exch}} + \mathbf{J}_{c,\text{mel}} + \mathbf{J}_{c,\text{dip}} + \mathbf{J}_{c,\text{ext}}$. For example, one has,

$$\mathbf{J}_{c,\text{mel}}(z, t) = -k_0(z)\mathbf{e}_s \times \left\{ \mathbf{m}^0 \times \left[\mathbf{m}^0 \times \mathbf{H}^{0,\text{mel}} + \alpha \mathbf{m}^0 \times (\mathbf{m}^0 \times \mathbf{H}^{0,\text{mel}}) \right] \right\}, \quad (14)$$

$$\mathbf{J}_{c,\text{exch}}(z, t) = -k_0(z)\mathbf{e}_s \times \left\{ \mathbf{m}^0 \times \left[\mathbf{m}^0 \times \mathbf{H}^{0,\text{exch}} + \alpha \mathbf{m}^0 \times (\mathbf{m}^0 \times \mathbf{H}^{0,\text{exch}}) \right] \right\}, \quad (15)$$

where the thickness-dependent pre-factor $k_0(z) = \alpha_{\text{SH}} \frac{e}{2\pi} \text{Re}[g_{\uparrow\downarrow}^r] \frac{\gamma}{1+\alpha^2} f(z)$; $\mathbf{H}^{0,\text{mel}}(t)$ and $\mathbf{H}^{0,\text{exch}}(t)$ refer to the magnetoelastic field and the magnetic exchange coupling field at the top surface of FeGa ($z=t_{\text{FeGa}}$). $\mathbf{H}^{0,\text{mel}}(t)$ is related to the temporal variation of local magnetization vector $\mathbf{m}^0(t)$ and the longitudinal strain $\varepsilon_{zz}^0(t)$. $\mathbf{H}^{0,\text{exch}}(t)$ is related to the variation of the second-order spatial derivative $\nabla^2 \mathbf{m}^0$. Expanding the x component of the Eqs. 14, dropping damping term $\alpha \mathbf{m}^0 \times (\mathbf{m}^0 \times \mathbf{H}^{0,\text{mel}})$ and plugging $(H_x^{\text{mel}}, H_y^{\text{mel}}, H_z^{\text{mel}}) = (0, 0, -\frac{2B_1}{\mu_0 M_s} m_z \varepsilon_{zz})$, one can derive a simplified formula for $\mathbf{J}_{c,\text{mel}}(z, t)$, the x -component of which is shown in Eq. (2). Likewise, for Eq. (15), expanding the x component, dropping damping term $\alpha \mathbf{m}^0 \times (\mathbf{m}^0 \times \mathbf{H}^{0,\text{exch}})$ and plugging $\mathbf{H}^{\text{exch}} = \frac{2A_{\text{ex}}}{\mu_0 M_s} \nabla^2 \mathbf{m}$, one has,

$$J_{c,x}^{\text{exch}}(z, t) \approx \frac{2A_{\text{ex}}}{\mu_0 M_s} k_0(z) \left[m_x^0 m_y^0 \frac{\partial^2 m_x^0}{\partial^2 z} - (m_x^{0^2} + m_z^{0^2}) \frac{\partial^2 m_y^0}{\partial^2 z} + m_y^0 m_z^0 \frac{\partial^2 m_z^0}{\partial^2 z} \right]. \quad (16)$$

By decomposing \mathbf{m}^0 into superimposed sinusoidal waves of different amplitudes $\Delta \mathbf{m}_q^0$, frequencies ω_q and wavenumbers k_q through Fourier transform, i.e., $\mathbf{m}^0(t) = \mathbf{m}_{\text{init}}^0 + \sum_q \Delta \mathbf{m}_q^0 e^{i(k_q z - \omega_q t)}$, one can obtain the explicit formulae of the second-order derivatives $\partial^2 \mathbf{m}^0 / \partial^2 z$. Furthermore, the time-varying \mathbf{m}^0 (precisely, m_x^0, m_y^0, m_z^0) in Eq. (16) can be approximated as $\mathbf{m}_{\text{init}}^0 = \mathbf{m}^0(t=0)$, in recognition of the fact that the absolute change in \mathbf{m}^0 is quite small (e.g., the absolute change in m_z is less than 0.001). Based on these, one can further expand Eq. (16) as,

$$J_{c,\text{exch}}^x(z, t) \approx -\frac{2A_{\text{ex}}}{\mu_0 M_s} k_0(z) \sum_q (\Delta \mathbf{m}_q^0 \cdot \mathbf{R}) k_q^2 e^{i(k_q z - \omega_q t)},$$

$$(\Delta \mathbf{m}_q^0 \cdot \mathbf{R}) = m_{\text{init},x}^0 m_{\text{init},y}^0 \Delta m_{q,x}^0 - \left((m_{\text{init},x}^0)^2 + (m_{\text{init},z}^0)^2 \right) \Delta m_{q,y}^0 + m_{\text{init},y}^0 m_{\text{init},z}^0 \Delta m_{q,z}^0. \quad (17)$$

$\mathbf{J}_c^{\text{anis}}$, $\mathbf{J}_c^{\text{dip}}$, and $\mathbf{J}_c^{\text{ext}}$ can likewise be evaluated, but their total contributions are often negligible because total effective field $\mathbf{H}^{0,\text{anis}} + \mathbf{H}^{0,\text{dip}} + \mathbf{H}^{0,\text{ext}}$ is initially along the direction of the magnetization at FeGa top surface $\mathbf{m}_{\text{init}}^0$ so that the magnetization is initially in equilibrium state, and the magnitudes of the temporal variation of $\mathbf{H}^{0,\text{anis}}$ and $\mathbf{H}^{0,\text{dip}}$ are only related to the temporal variation of $\mathbf{m}^0(t)$, which are therefore negligible as well, hence, the torque $\mathbf{m}^0 \times (\mathbf{H}^{0,\text{anis}} + \mathbf{H}^{0,\text{dip}} + \mathbf{H}^{0,\text{ext}})$ is negligibly small due to nearly parallelization of the direction of \mathbf{m}^0 and the total effective field $\mathbf{H}^{0,\text{anis}} + \mathbf{H}^{0,\text{dip}} + \mathbf{H}^{0,\text{ext}}$, leading to their negligible total contribution to the charge current.

Calculation of the emitted THz electric field

The time-changing charge current $\mathbf{J}_c(\mathbf{r},t)$ in the Pt generates electromagnetic waves in the free space. The free-space electric-field component of the electromagnetic wave is calculated as $\mathbf{E}(\mathbf{r},t) = -\frac{\partial \mathbf{A}(\mathbf{r},t)}{\partial t}$, where $\mathbf{A}(\mathbf{r},t) = \frac{\mu_0}{4\pi} \int \frac{\mathbf{J}_c(\mathbf{r}',t-|\mathbf{r}-\mathbf{r}'|/c)}{|\mathbf{r}-\mathbf{r}'|} d^3\mathbf{r}'$, of electromagnetic waves radiation,⁵⁵ where \mathbf{r} and \mathbf{r}' denote field points and source points, c is the speed of light in vacuum. Because Pt layer is only 5-nm-thick, the integration of charge current density over entire volume of Pt layer can be approximated as the integration of surface charge current density over the top surface of Pt, i.e., $\int \frac{\mathbf{J}_c(\mathbf{r}',t-|\mathbf{r}-\mathbf{r}'|/c)}{|\mathbf{r}-\mathbf{r}'|} d^3\mathbf{r}' = \int \frac{\mathbf{K}_c(\mathbf{r}',t-|\mathbf{r}-\mathbf{r}'|/c)}{|\mathbf{r}-\mathbf{r}'|} d^2\mathbf{r}'$. Assuming $\mathbf{J}_c(\mathbf{r},t)$ is spatially uniform in the xy plane, one has $\mathbf{K}_c(\mathbf{r},t) = \mathbf{J}_c^0(t) \int_{t_{\text{Pt}}}^{t_{\text{Pt}}+t_{\text{FeGa}}} \frac{\sinh\left(\frac{t_{\text{FeGa}}+t_{\text{Pt}}-z}{l_{sd}}\right)}{\sinh\left(\frac{t_{\text{Pt}}}{l_{sd}}\right)} dz$. The $\mathbf{E}(\mathbf{r},t)$ at the center point of the top surface of Pt layer is taken as $E_{\text{THz}}(t)$, and the x -component of $E_{\text{THz}}(t)$ is presented in Fig. 6a.

Experimental evaluation of thin film FeGa parameters

Thin film 001-oriented Fe_{79.5}Ga_{20.5} (FeGa) was deposited from a stoichiometric target via pulsed laser deposition (PLD). The film was deposited epitaxially on a single-crystalline, 001-oriented MgO substrate at 200°C and a 20 mTorr Ar backing pressure. Epitaxy was confirmed with θ -2 θ X-ray diffraction and asymmetric ϕ scan of the FeGa/MgO heterostructure (Supplementary Information 1). In-plane angle dependent magnetic hysteresis loops show a clear magnetocrystalline anisotropy (Fig. S1c). The anisotropy constant K_1 was extracted from experimental measurements along the sample 110 and 100 crystallographic directions by integration of magnetic hysteresis loops (Fig. S1d) according to $A_{ijk} = \int_0^{H(M_S)} M dH$ in order to

extract the energy lost during magnetization reorientation. This can then be used to calculate the anisotropy energy K_1 through $A_{110} - A_{100} = K_1/4$.

Figures and Captions

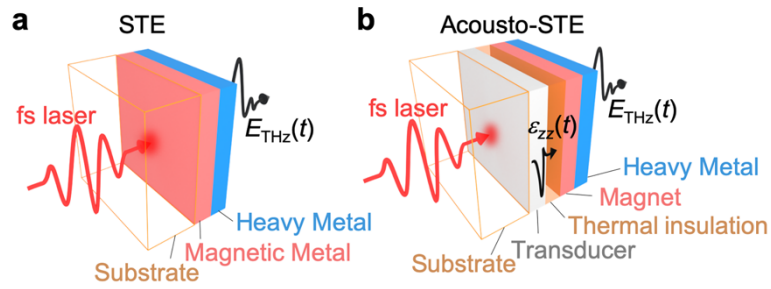


Figure 1. Device Structure. **a**, Schematic of a spintronic THz emitter (STE) which can convert a near-infrared femtosecond (fs) laser pulse into an ultra-broadband THz pulse with bandwidths ranging from 0.6 to 30 THz. **b**, Schematic of the proposed acoustically mediated STE (acousto-STE), which can convert the same fs laser pulse into an ultra-narrowband THz pulse with a bandwidth of ~ 0.01 THz, mediated by a laser-induced picosecond acoustic strain pulse $\varepsilon_{zz}(t)$.

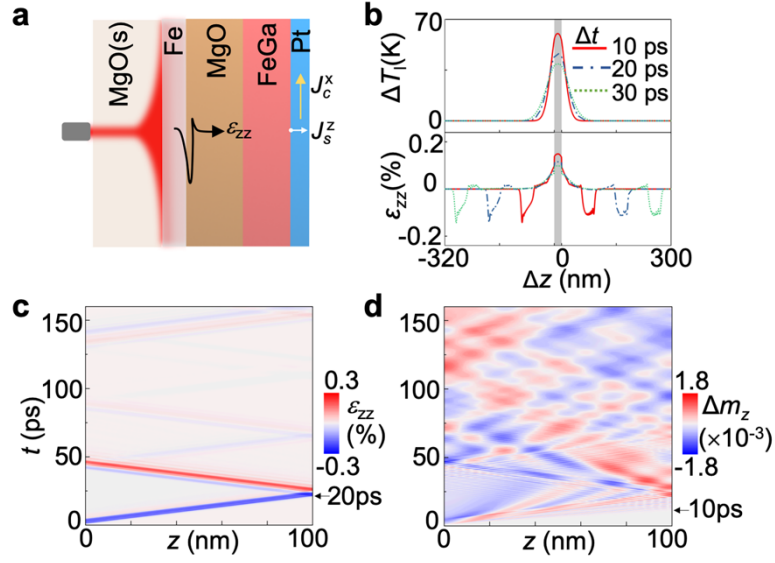


Figure 2. Optical excitation of elastic waves and spin waves in FeGa. (a) Schematic (side view) of the acousto-STE. Magnetization precession at the top FeGa surface leads to the injection of a spin current (white arrow) into the Pt, where it is converted to a charge current (yellow arrow) that in turn delivers THz emission (not plotted). (b) Profiles of the lattice temperature rise ΔT_l (top) and strain ϵ_{zz} (bottom) across the thickness direction of (from left to right) MgO(substrate)/Fe/MgO(film) at $\Delta t = 10$ ps, 20 ps, and 30 ps. Here $\Delta t = 0$ ps is defined as the moment when laser pumping starts. The shaded area indicates the Fe layer. Propagation of the longitudinal elastic wave (c) and spin wave (d) between the bottom ($z=0$ nm) and top ($z=100$ nm) surfaces of FeGa. Note that $\Delta m_z = m_z(z,t) - m_z(z,t=0)$ is evaluated using the m_z at $t=0$ ps as the reference, where $t=0$ ps is defined as the moment when the acoustic wave arrives at the FeGa bottom surface for the first time.

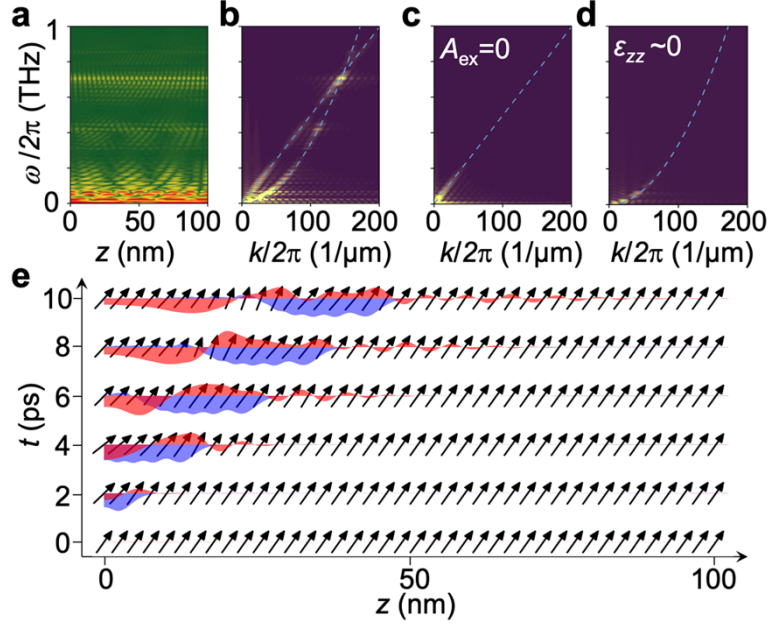


Figure 3. Mechanisms of spin wave excitation in FeGa. **a**, Spatially resolved frequency spectra of the longitudinal spin wave $\Delta m_z(z,t)$ in the FeGa from $t=0$ ps to $t=160$ ps. **b**, Corresponding frequency-wavenumber relationship $\omega(k)$. **c,d**, Control simulations where the $\omega(k)$ relationship is obtained under zero exchange coupling coefficient A_{ex} (a pure elastic excitation), or within a different time period (from $t=70$ ps to $t=125$ ps) during which the ε_{zz} is negligibly small (hence a pure exchange-coupling based excitation). **e**, the propagation of elastic wave and excitation of spin wave in the FeGa from $t=0$ ps to $t=10$ ps. The elastic and spin waves are represented by blue and red shades, and the wave amplitude scales with the ε_{zz} and Δm_z , respectively. The arrows indicate local magnetization vectors, whose tilting angles are amplified by 160 times for clarity.

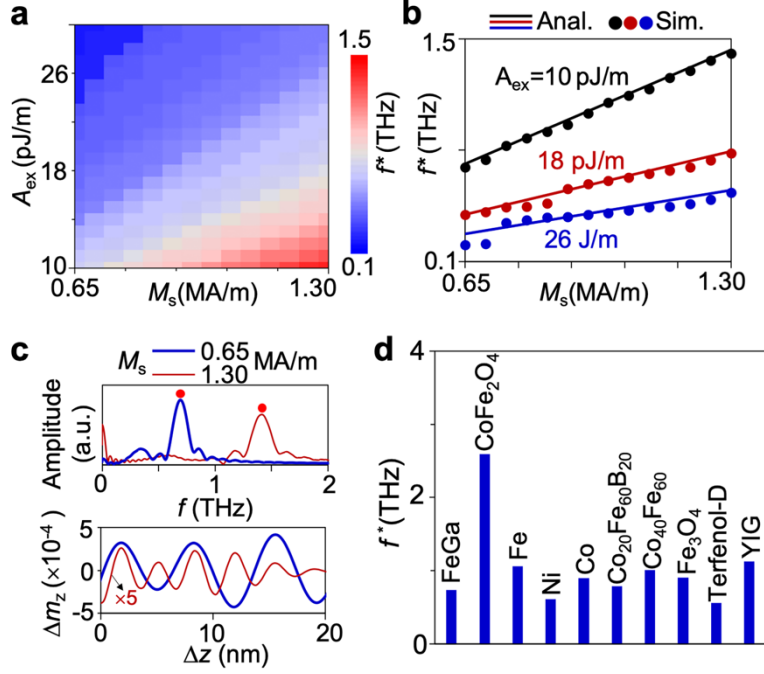


Figure 4. Tuning the center frequency f^* of high-frequency exchange spin wave in FeGa. **a**, Density map of f^* as a function of the exchange coupling coefficient A_{ex} and saturation magnetization M_s , obtained by numerical simulations. **b**, Line plots of f^* under different A_{ex} , obtained by both numerical simulations and analytical formula (Eq. 1). **c**, (Top) frequency spectra of these high-frequency exchange spin waves that are initiated by the elastic wave, obtained under two different M_s but the same A_{ex} of 10 pJ/m; (Bottom) their temporal waveforms at the same moment. For $M_s=1.3\text{MA/m}$ (red line), the magnitude of Δm_z is amplified by 5 times for clarity. **d**, center frequency f^* in common magnetoelastic materials.

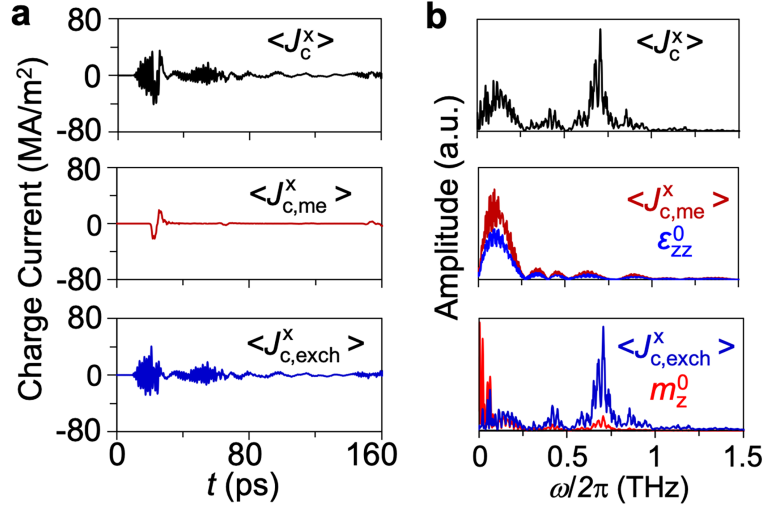


Figure 5. Charge current excitation in Pt. **a**, Temporal evolution of the x -component of the average charge current $\langle J_c^x \rangle$ in Pt and the contribution from the magnetoelastic and exchange coupling, denoted as $\langle J_{c,me}^x \rangle$ and $\langle J_{c,exch}^x \rangle$, respectively. **b**, Frequency spectra of the $\langle J_c^x \rangle(t)$, $\langle J_{c,me}^x \rangle(t)$ and $\epsilon_{zz}^0(t)$, and $\langle J_{c,exch}^x \rangle(t)$ and $m_z^0(t)$. Here the $\epsilon_{zz}^0(t)$ and $m_z^0(t)$ refer to the temporal variation of the strain and magnetization at the FeGa top interface, respectively.

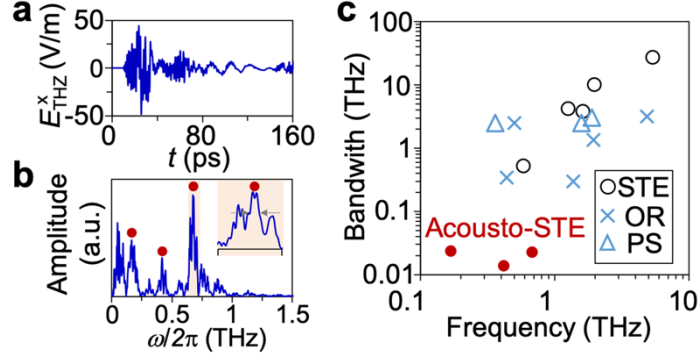


Figure 6. Narrowband THz emission. **a**, the electric-field component of the emitted THz electromagnetic radiation $E_{\text{THz}}(t)$ and **b**, its Fourier frequency spectra of the proposed acoustically mediated spintronic THz emitter (acousto-STE). Three highest peaks in the THz regime are indicated. The bandwidth is determined from the full width at half maximum of individual peaks (inset). **c**, Peak frequencies and bandwidths of the acousto-STE, conventional STE, and other fs-laser-excited THz emitters which operate based on a photoconductive switch (PS) such as GaAs, InAs and their solid-solution^{9–11}; or the optical rectification effect in semiconductors (ZnTe, GaP) and nonlinear crystals (LiNbO₃, DAST)^{9,12,13}.

References

1. Ferguson, B. & Zhang, X.-C. Materials for terahertz science and technology. *Nat. Mater.* **1**, 26–33 (2002).
2. Auston, D. H., Cheung, K. P., Valdmanis, J. A. & Kleinman, D. A. Cherenkov Radiation from Femtosecond Optical Pulses in Electro-Optic Media. *Phys. Rev. Lett.* **53**, 1555–1558 (1984).
3. Fattinger, C. & Grischkowsky, D. Point source terahertz optics. *Appl. Phys. Lett.* **53**, 1480–1482 (1988).
4. Horiuchi, N. & Zhang, X.-C. Bright terahertz sources. *Nat. Photonics* **7**, 670 (2013).
5. Tonouchi, M. Cutting-edge terahertz technology. *Nat. Photonics* **1**, 97 (2007).
6. Hu, B. B. & Nuss, M. C. Imaging with terahertz waves. *Opt. Lett.* **20**, 1716–1718 (1995).
7. Mittleman, D. M. Frontiers in terahertz sources and plasmonics. *Nat. Photonics* **7**, 666 (2013).
8. Kawase, K., Ogawa, Y., Watanabe, Y. & Inoue, H. Non-destructive terahertz imaging of illicit drugs using spectral fingerprints. *Opt. Express* **11**, 2549–2554 (2003).
9. Seifert, T. *et al.* Efficient metallic spintronic emitters of ultrabroadband terahertz radiation. *Nat. Photonics* **10**, 483 (2016).
10. Klatt, G. *et al.* Terahertz emission from lateral photo-Dember currents. *Opt. Express* **18**, 4939–4947 (2010).
11. Matthäus, G. *et al.* Surface-emitted THz generation using a compact ultrashort pulse fiber amplifier at 1060nm. *Opt. Commun.* **261**, 114–117 (2006).
12. Hoffmann, M. C., Yeh, K.-L., Hebling, J. & Nelson, K. A. Efficient terahertz generation by optical rectification at 1035 nm. *Opt. Express* **15**, 11706–11713 (2007).
13. Schneider, A. *et al.* Generation of terahertz pulses through optical rectification in organic DAST crystals: theory and experiment. *J. Opt. Soc. Am. B* **23**, 1822–1835 (2006).
14. Kampfrath, T. *et al.* Terahertz spin current pulses controlled by magnetic heterostructures. *Nat. Nanotechnol.* **8**, 256 (2013).
15. Huisman, T. J. *et al.* Femtosecond control of electric currents in metallic ferromagnetic heterostructures. *Nat. Nanotechnol.* **11**, 455 (2016).
16. Yang, D. *et al.* Powerful and Tunable THz Emitters Based on the Fe/Pt Magnetic Heterostructure. *Adv. Opt. Mater.* **4**, 1944–1949 (2016).
17. Wu, Y. *et al.* High-Performance THz Emitters Based on Ferromagnetic/Nonmagnetic Heterostructures. *Adv. Mater.* **29**, 1603031 (2017).
18. Sasaki, Y., Suzuki, K. Z. & Mizukami, S. Annealing effect on laser pulse-induced THz wave emission in Ta/CoFeB/MgO films. *Appl. Phys. Lett.* **111**, 102401 (2017).

19. Torosyan, G., Keller, S., Scheuer, L., Beigang, R. & Papaioannou, E. T. Optimized Spintronic Terahertz Emitters Based on Epitaxial Grown Fe/Pt Layer Structures. *Sci. Rep.* **8**, 1311 (2018).
20. Jungfleisch, M. B. *et al.* Control of Terahertz Emission by Ultrafast Spin-Charge Current Conversion at Rashba Interfaces. *Phys. Rev. Lett.* **120**, 207207 (2018).
21. Seifert, T. *et al.* Ultrabroadband single-cycle terahertz pulses with peak fields of 300 kV cm⁻¹ from a metallic spintronic emitter. *Appl. Phys. Lett.* **110**, 252402 (2017).
22. Seifert, T. S. *et al.* Terahertz spectroscopy for all-optical spintronic characterization of the spin-Hall-effect metals Pt, W and Cu₈₀Ir₂₀. *J. Phys. D: Appl. Phys.* **51**, 364003 (2018).
23. Battiato, M., Carva, K. & Oppeneer, P. M. Superdiffusive Spin Transport as a Mechanism of Ultrafast Demagnetization. *Phys. Rev. Lett.* **105**, 27203 (2010).
24. Battiato, M., Carva, K. & Oppeneer, P. M. Theory of laser-induced ultrafast superdiffusive spin transport in layered heterostructures. *Phys. Rev. B* **86**, 24404 (2012).
25. Saitoh, E., Ueda, M., Miyajima, H. & Tataru, G. Conversion of spin current into charge current at room temperature: Inverse spin-Hall effect. *Appl. Phys. Lett.* **88**, 182509 (2006).
26. Seifert, T. *et al.* Terahertz Spin Currents and Inverse Spin Hall Effect in Thin-Film Heterostructures Containing Complex Magnetic Compounds. *SPIN* **07**, 1740010 (2017).
27. Huisman, T. J. *et al.* Spin-photo-currents generated by femtosecond laser pulses in a ferrimagnetic GdFeCo/Pt bilayer. *Appl. Phys. Lett.* **110**, 72402 (2017).
28. Schneider, R. *et al.* Magnetic-Field-Dependent THz Emission of Spintronic TbFe/Pt Layers. *ACS Photonics* **5**, 3936–3942 (2018).
29. Tas, G. & Maris, H. J. Electron diffusion in metals studied by picosecond ultrasonics. *Phys. Rev. B* **49**, 15046–15054 (1994).
30. Tserkovnyak, Y., Brataas, A. & Bauer, G. E. W. Enhanced Gilbert Damping in Thin Ferromagnetic Films. *Phys. Rev. Lett.* **88**, 117601 (2002).
31. Parkes, D. E. *et al.* Magnetostrictive thin films for microwave spintronics. *Sci. Rep.* **3**, 2220 (2013).
32. Jäger, J. V. *et al.* Picosecond inverse magnetostriction in galferol thin films. *Appl. Phys. Lett.* **103**, 32409 (2013).
33. Mosendz, O. *et al.* Detection and quantification of inverse spin Hall effect from spin pumping in permalloy/normal metal bilayers. *Phys. Rev. B* **82**, 214403 (2010).
34. Beaurepaire, E. *et al.* Coherent terahertz emission from ferromagnetic films excited by femtosecond laser pulses. *Appl. Phys. Lett.* **84**, 3465–3467 (2004).
35. Gusev, V. E. & Wright, O. B. Ultrafast nonequilibrium dynamics of electrons in metals. *Phys. Rev. B* **57**, 2878–2888 (1998).
36. Zhao, G., Schouten, R. N., van der Valk, N., Wenckebach, W. T. & Planken, P. C. M. Design and performance of a THz emission and detection setup based on a semi-insulating

- GaAs emitter. *Rev. Sci. Instrum.* **73**, 1715–1719 (2002).
37. Blanchard, F. *et al.* Generation of 1.5 μJ single-cycle terahertz pulses by optical rectification from a large aperture ZnTe crystal. *Opt. Express* **15**, 13212–13220 (2007).
 38. Lenk, B., Ulrichs, H., Garbs, F. & Münzenberg, M. The building blocks of magnonics. *Phys. Rep.* **507**, 107–136 (2011).
 39. Azotsev, A. V & Pertsev, N. A. Coupled magnetic and elastic dynamics generated by a shear wave propagating in ferromagnetic heterostructure. *Appl. Phys. Lett.* **111**, 222403 (2017).
 40. Uchida, K. *et al.* Long-range spin Seebeck effect and acoustic spin pumping. *Nat. Mater.* **10**, 737 (2011).
 41. Henighan, T. *et al.* Generation mechanism of terahertz coherent acoustic phonons in Fe. *Phys. Rev. B* **93**, 220301 (2016).
 42. Azotsev, A. V & Pertsev, N. A. Dynamical spin phenomena generated by longitudinal elastic waves traversing CoFe_2O_4 films and heterostructures. *Phys. Rev. B* **100**, 224405 (2019).
 43. Predel, B. Ac-Ag ... Au-Zr · Introduction. in *SpringerMaterials* (ed. Predel, B.) (Springer-Verlag Berlin Heidelberg). doi:10.1007/10793176_2
 44. Kittel, C. *Introduction to solid state physics 8th ed.* (John Wiley & Sons, Inc., 2005).
 45. Lin, Z., Zhigilei, L. V & Celli, V. Electron-phonon coupling and electron heat capacity of metals under conditions of strong electron-phonon nonequilibrium. *Phys. Rev. B* **77**, 75133 (2008).
 46. Leese, J. & Lord, A. E. Elastic Stiffness Coefficients of Single-Crystal Iron from Room Temperature to 500°C. *J. Appl. Phys.* **39**, 3986–3988 (1968).
 47. Desai, P. D. Thermodynamic Properties of Iron and Silicon. *J. Phys. Chem. Ref. Data* **15**, 967–983 (1986).
 48. Powell, R. W. Further measurements of the thermal and electrical conductivity of iron at high temperatures. *Proc. Phys. Soc.* **51**, 407–418 (1939).
 49. Nix, F. C. & MacNair, D. The Thermal Expansion of Pure Metals: Copper, Gold, Aluminum, Nickel, and Iron. *Phys. Rev.* **60**, 597–605 (1941).
 50. Sumino, Y., Anderson, O. L. & Suzuki, I. Temperature coefficients of elastic constants of single crystal MgO between 80 and 1,300 K. *Phys. Chem. Miner.* **9**, 38–47 (1983).
 51. Hofmeister, A. M. Thermal diffusivity and thermal conductivity of single-crystal MgO and Al_2O_3 and related compounds as a function of temperature. *Phys. Chem. Miner.* **41**, 361–371 (2014).
 52. Clark, A. E. *et al.* Extraordinary magnetoelasticity and lattice softening in bcc Fe-Ga alloys. *J. Appl. Phys.* **93**, 8621–8623 (2003).
 53. Collard, S. M. & McLellan, R. B. High-temperature elastic constants of platinum single

- crystals. *Acta Metall. Mater.* **40**, 699–702 (1992).
54. Rojas-Sánchez, J.-C. *et al.* Spin Pumping and Inverse Spin Hall Effect in Platinum: The Essential Role of Spin-Memory Loss at Metallic Interfaces. *Phys. Rev. Lett.* **112**, 106602 (2014).
 55. Pollack, G. L. & Stump, D. R. *Electromagnetism*. (Addison Wesley, 2005).